An Automated Initialization System for Robust Model-Based Segmentation of Lungs in CT Data

Gurman Gill[1,3], Matthew Toews[4], and Reinhard R Beichel[1,2,3]

[1] Dept. of Electrical and Computer Engineering
[2] Dept. of Internal Medicine
[3] The Iowa Institute for Biomedical Imaging
The University of Iowa, Iowa City, IA 52242, USA
{gurman-gill,reinhard-beichel}@uiowa.edu
[4] Brigham and Womens Hospital, Harvard Medical School,
mt@bwh.harvard.edu

Abstract. In this paper we study the feasibility of an automated initialization system for a robust model-based lung segmentation approach. The lung segmentation method consists of a robust active shape model (RASM) matching stage followed by an optimal surface finding step. The RASM needs to be initialized in rough proximity to the target structure for achieving good segmentation results. For this purpose we employ a feature-based alignment (FBA) method to predict three landmark points (lung apex and carina). These landmark points are subsequently used to calculate initial model parameters. The approach was evaluated on a diverse set of 98 CT scans of normal and diseased lungs by comparison to an independent reference standard. For segmentation results based on the new initialization approach, the mean and standard deviation of the Dice coefficient was 0.976 ± 0.025. In comparison, the Dice coefficient of lung segmentations based on the previously utilized initialization method was 0.971 ± 0.040. The new RASM initialization approach is 3-times faster than the previously utilized method and can be expanded by including additional landmarks.

Keywords: Lung segmentation, computed tomography, model initialization

1 Introduction

Segmentation of lungs in CT scans often serves as a first step for quantitative lung image analysis. Most approaches exploit the large density difference between air-filled lung parenchyma and surrounding tissues for segmenting lungs [3][2][4]. However, these methods can fail on diseased lungs where the expected density difference is not observed. Recently, different methods have been developed to deal with this issue. Approaches range from employing an error-correcting hybrid system [10], a combination of feature-based and threshold-based segmentations [11], a registration methods [6], and a shape "break-and-repair" system [5].

In [8], we have presented a fully automated Robust Active Shape Model (RASM) based method that address the issue of segmenting lungs with large high density structures like lung tumors. It utilizes an active shape model (ASM) [1] of lungs generated from a training set and employs a robust model matching method for fitting the lung model to CT images of lungs. In a subsequent step, the RASM segmentation is automatically refined by means of an optimal surface segmentation method [8].

In general, ASM based methods work well when they are initialized in proximity to the target structure, because of the limited capture range of ASM's (i.e., profile length). Consequently, initialization of the RASM is an important step in fitting the lung model to a new CT volume. For this purpose, initial RASM shape b and pose T (i.e., location, scale and rotation) parameters need to be determined. Our previous initialization method reported in [8] utilized the mean shape ($b = 0$) and automatically derived the pose parameters based on a rib detection step. Specifically, the location and isotropic scale were calculated using the bounding box of the ribcage, assuming that ribs are a good predictor for the location of the lungs. We found that this assumption holds for many cases, as demonstrated in [8] (Fig. 1a). However, this initialization system is dependent on an accurate segmentation of the ribs. If several ribs are not detected correctly due to low bone density or other factors, the derived location and scale estimate can be off (Fig. 1b). In addition, lungs may be scanned using CT protocol that covers area up until the abdomen. When compared to rib-cage, these lungs appear much shorter and can cause initialization problems (Fig. 1c).

In this paper, we investigate an alternative approach for fully automated RASM initialization, which is based on an estimate of landmark points in a lung CT scans. The method is validated on a set of 98 MDCT lung scans containing 49 TLC and 49 FRC images, which represents a mixture of normal and diseased lungs. In addition to a performance analysis, we provide a detailed comparison to our old initialization approach reported in [8].

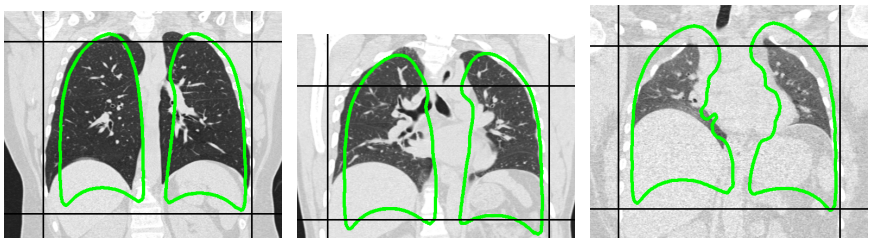

(a) (b) (c)

Fig. 1: TLC images showing the rib-cage bounding box along with the associated initial ASM for three different cases: a) Correct ribs, b) Incorrect ribs, c) Correct ribs but a different CT scanning protocol. Note: scale here is computed isotropically based only on x and y extent of rib-cage [8].

2 Methods

Our approach to initialization of our robust lung segmentation method [8] is based on two main processing steps. First, given a new lung CT data set to process, three key landmark points are estimated by utilizing a feature-based alignment approach. Second, based on these landmark points, initial RASM pose parameters are calculated. A detailed description of these two steps is given in the following subsections.

2.1 Estimation of Landmark Points

The aim is to select landmarks that can be estimated even in presence of diseases and/or failure of conforming to CT protocol. Here we utilize three different landmark points, namely left-lung apex, right-lung apex and carina (Fig. 2). These points are chosen since they would be least affected by lung diseases. For landmark estimation, a feature-based model is learnt from a set of 50 training images of normal lungs. The three landmark points are labeled in each training image. The aim is to learn a model which can be used to predict the location of these landmarks in a new lung CT image volume. This task is complicated by a variety of factors including inter-subject anatomical variability, particularly in the case of disease, subject misalignment, etc. A variety of localization techniques could be brought to bear, here we adopt the feature-based alignment (FBA) method [9].

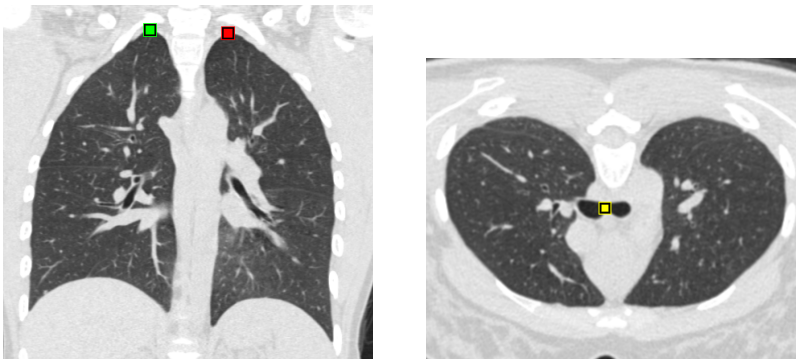

(a) (b)

Fig. 2: Typical locations of lung apex and carina. (a) Frontal view showing apex. (b) Axial view showing carina.

FBA makes use of local 3D scale-invariant feature representation, whereby image volumes are transformed into a collection of distinctive local image patches, each consisting of a location, scale and 3D orientation. The locations and scales of patches or features are identified based on the multi-scale difference-of-Gaussian

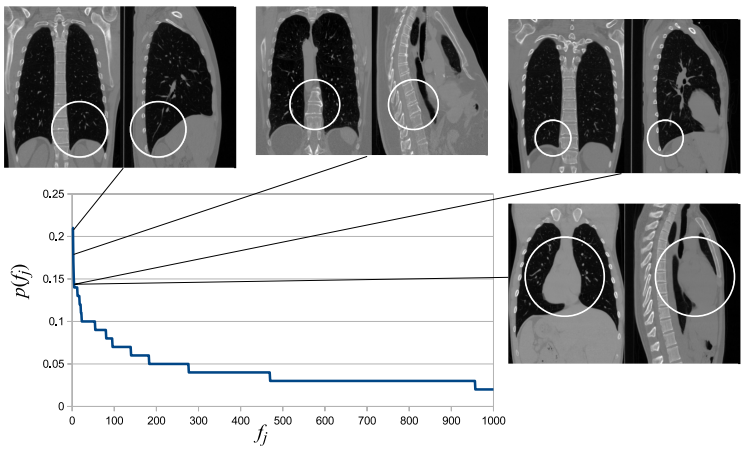

Fig. 3: Illustrating the feature-based model derived from lung CT volumes. The graph plots the occurrence probability $p(f_i)$ of distinct scale-invariant features f_i. Several examples of relatively common features are shown, circles indicate the location and scale of prototype features. Note that occurrence probabilities are relatively low, this is because the same anatomical region may not be identifiable in all subjects (e.g. due to disease) or may be represented by different model features.

operator, after which 3D orientations are assigned to each feature based on dominant image gradients computed within the patch. Once feature geometry has been defined, image patches are cropped, normalized according to their geometry and encoded using the gradient orientation histogram appearance descriptor.

Let T represent a similarity transform from a subject to a normalized reference space, and let $I = \{I_1, \ldots, I_i, \ldots\}$ represent a set of features extracted in an image. FBA models the posterior probability of the transform aligning I to a set of latent model features $\{f_1, \ldots, f_j, \ldots\}$:

$$p(T|I) \propto p(T)p(I|T) = p(T) \prod_i \sum_j p(I_i|f_j, T)p(f_j). \quad (1)$$

In Equation (1), $p(I_i|f_j, T)$ represents a conditional density over extracted feature parameters (i.e. geometry and appearance descriptor), $p(f_j)$ represents the occurrence probability of latent feature instance f_j and $p(T)$ is a prior density over transform T. Density and probability parameters are estimated from feature data extracted in a set of aligned training images, resulting in a feature-based model or atlas. This is achieved via a robust clustering process, identifying sets of features across subjects that are similar in terms of their geometry and appearance. Each such cluster represents a set of different instances of the same underlying anatomical pattern f_j in different subjects, from which probability and density parameters are estimated via maximum likelihood. Figure 3 illus-

trates the feature-based model, including feature occurrence probabilities $p(f_j)$ and several prototype features f_j.

FBA aligns all training images into a model reference frame based on matching features. To define the location of landmark points in the model framework, all training landmark points need to be mapped to the model reference frame. The average of the training label coordinates λ in the model reference frame represents the location of landmark points in the model framework.

Given a new test image, features can be extracted and aligned to the feature-based model by maximizing a-posteriori similarity transform $p(T|I)$:

$$T_{MAP} = \underset{T}{\operatorname{argmax}}\{p(T|I)\} \tag{2}$$

Note an uninformative uniform prior probability $p(T)$ is used in equation 2. The alignment solution consists of T_{MAP} in addition to locally linear deformations between corresponding image and model features. The advantages of FBA system are efficiency and robustness; computation time is approximately 40 seconds (primarily due to feature extraction), and alignment can be achieved despite arbitrary global similarity transforms.

Once the new test image is aligned to the model, predicting the location of the landmarks is thereafter straightforward. The mean landmark locations λ in model reference frame are simply transformed via T_{MAP}^{-1} to identify their locations in test subject space.

2.2 Calculation of RASM Pose Parameters

Since we have independent models for right and left lungs [8], RASM initialization and segmentation is done independently for them. Initializing a RASM requires specifying the initial shape and pose parameters. Similar to our previous work [8], we use the mean shape parameters to get the initial shape. The pose parameters, specifically the isotropic scale parameter s and location parameter $\boldsymbol{l} = (l_x, l_y, l_z)$, are derived from the three landmarks whose estimate is provided by the method described in section 2.1. Note that just like in [8] the rotation parameter was not required to be calculated due to the utilized CT protocol.

Let the lung apex be denoted by $\boldsymbol{a} = (a_x, a_y, a_z)$ and carina by $\boldsymbol{c} = (c_x, c_y, c_z)$. The components of initial location parameter $\boldsymbol{l}$ of RASM are computed independently from the coordinates of lung apex $\boldsymbol{a}$ and carina $\boldsymbol{c}$. Consider the figure 4 showing apex and carina overlaid on a slice of CT image in both axial and frontal view. This will serve as a template for series of empirical observations.

In the x-direction (Fig. 4a), it is observed that the center of each lung can be computed as an offset from c_x. This offset can be determined using the difference between each lung apex and carina in x-direction. In the y-direction, the location of carina c_y forms a robust estimator for l_y. Lastly, in the z-direction, the geometric center of lung can be computed as an offset from c_z (Fig. 4b). This offset can be determined using the difference between the lung apex and

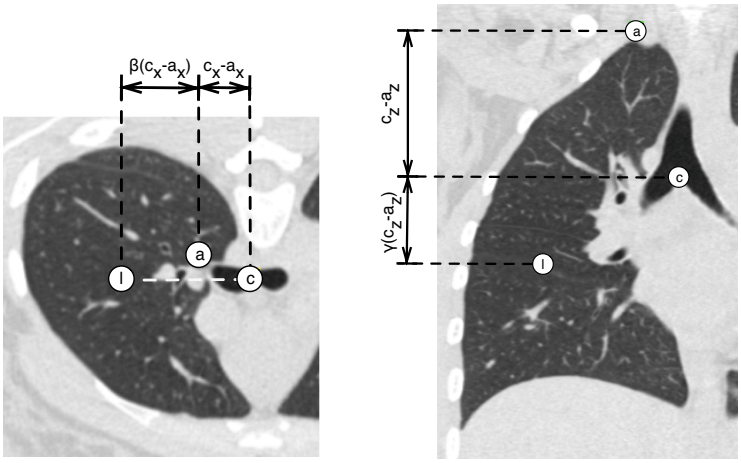

(a) (b)

Fig. 4: Diagram showing relationship of location $\boldsymbol{l}$ to apex $\boldsymbol{a}$ and carina $\boldsymbol{c}$

carina in z-direction. Based on all these observations, we define the location $\boldsymbol{l}$ as

$$\begin{aligned} l_x &= c_x + \beta(c_x - a_x) \\ l_y &= c_y \\ l_z &= c_z + \gamma(c_z - a_z) \end{aligned} \tag{3}$$

where we experimentally determine $\beta = 1.5$ and $\gamma = 0.667$.

To compute the isotropic scale parameter s, we observe that the distance from lung apex to carina is a good indicator of the size of lungs. In other words, longer lungs tend to have a higher apex-to-carina distance and shorter lungs have this distance smaller. This observation is made for lungs across different subjects. Based on this, $s \propto c_z - a_z$. Denoting the apex and carina of the mean shape, respectively, by $\boldsymbol{a}^*$ and $\boldsymbol{c}^*$, the scale for initial ASM can be written as

$$s = \frac{c_z - a_z}{c_z^* - a_z^*} \tag{4}$$

Note that relationships given in equation 3 and 4 will be slightly different for TLC and FRC images. Specifically, the scale s will be smaller for FRC images. And the location offset in z-direction, given by γ, will also be smaller. Here we attempt to automatically initialize the RASM without a priori information regarding the breathing state and use the same parameters for both TLC and FRC images. The motivation for doing this is to be able to account for non-compliance during imaging or lung disease such as COPD.

Figure 5 shows these points and the initial RASM for some images. Based on this initialization, RASM-OSF based segmentation procedure [8] is applied to segment the left and right lungs. Thereafter, the segmentation performance is

measured relative to the reference segmentations. In the next section, we describe the experimental setup, test and reference data, and the evaluation measure used to compare the performance.

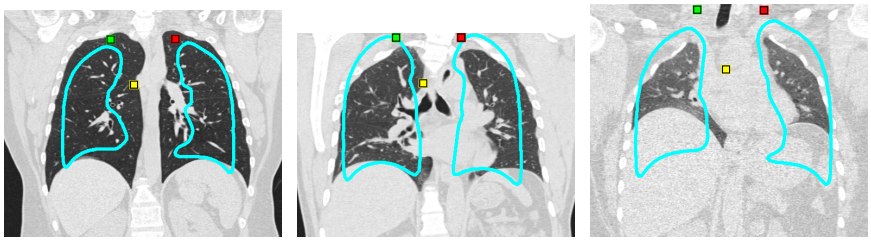

(a) (b) (c)

Fig. 5: Images showing projection of the three landmarks along with the associated initial ASM. Compare with figure 1.

3 Evaluation

3.1 Image Data

For evaluation, 98 multidetector computed tomography (MDCT) thorax scans were utilized. The scans were partitioned into four different sets as follows. Sets S_{normal}, S_{asthma}, S_{copd}, and S_{mix} represent MDCT scans of lungs with no significant abnormalities (normals), asthma (both severe and non-severe), COPD (GOLD 1 to 4), and a mix of different lung diseases (e.g., IPF, COPD, etc.), respectively. Each set contains scans of the same person at TLC and FRC. The total number of scans in sets S_{normal}, S_{asthma}, S_{copd} and S_{mix} are, respectively, 20, 24, 28 and 26. The image sizes vary from $512 \times 512 \times 415$ to $512 \times 512 \times 642$ voxels. The slice thickness of images ranged from 0.5 mm to 0.6 mm and the in-plane resolution from 0.55×0.55 mm to 0.71×0.71 mm.

3.2 Experimental Setup

Active shape models were created for left and right lung shapes using a combination of 75 TLC and 75 FRC scans of normal lungs. The models were then robustly fitted to the test CT scans (Section 3.1) to segment the left and right lungs. Details about model generation and matching can be found in [8]; the only difference was the method utilized for automatic initialization of the RASM.

For Method 1, the rib-based automated initialization system reported in [8] was used. In the case of Method 2, the landmark-based initialization system described in Section 2 was applied.

Table 1: Overall Lung Segmentation Results for Initialization Methods 1 and 2.

Set	State	$D_{Method1}$	$D_{Method2}$
S_{normal}	TLC	**0.989 ± 0.002**	0.988 ± 0.002
	FRC	0.981 ± 0.006	**0.982 ± 0.004**
S_{asthma}	TLC	**0.982 ± 0.009**	0.981 ± 0.014
	FRC	0.947 ± 0.069	**0.971 ± 0.016**
S_{copd}	TLC	0.986 ± 0.007	**0.986 ± 0.005**
	FRC	0.960 ± 0.062	**0.977 ± 0.013**
S_{mix}	TLC	**0.975 ± 0.018**	0.973 ± 0.031
	FRC	**0.954 ± 0.040**	0.948 ± 0.045
Overall		0.971 ± 0.040	**0.976 ± 0.025**

3.3 Independent Reference and Quantitative Index

For all test data sets, an independent reference standard was generated by using the commercial lung image analysis software package Apollo (VIDA Diagnostics Inc., Coralville, IA) to automatically create lung segmentations. These were then inspected by an expert and segmentation errors were manually corrected, if needed. The dice coefficient D [7] was utilized to measure the segmentation accuracy of the lung segmentations compared to the independent reference standard.

4 Results

Table 1 summarizes the Dice coefficient for Methods 1 and 2 on the 98 test data sets. Figure 6 shows the bar plot of the difference $D_{Method2} - D_{Method1}$ to better highlight performance differences between both approaches. To assess the effect of the initialization method on the first processing step of our lungs segmentation method, the Dice coefficient for the intermediate RASM matching results was calculated. It was 0.941 ± 0.041 and 0.946 ± 0.029 for method 1 and 2, respectively. As reported in [8], the required computing time was for Method 1 was 2 min on average. In comparison, Method 2 required 40 seconds on average.

A comparison of segmentation results achieved after the RASM step for both initialization methods is given in Fig. 7. If the initial RASM is far-away from the target structure, the RASM matching fails and OSF refinement can't recover from it sometimes. Figure 8 shows the segmentation results achieved after the OSF step for both initialization methods.

Method 2 primarily shows failure in 3 cases, all belonging to the S_{mix} set. These primarily failed due to applying the same location/scale estimates (see eq. 3 and 4) for both TLC and FRC lungs. This assumption along with incorrect predictions for landmark points can result in incorrect placement of the RASM. Figure 9 shows one such case.

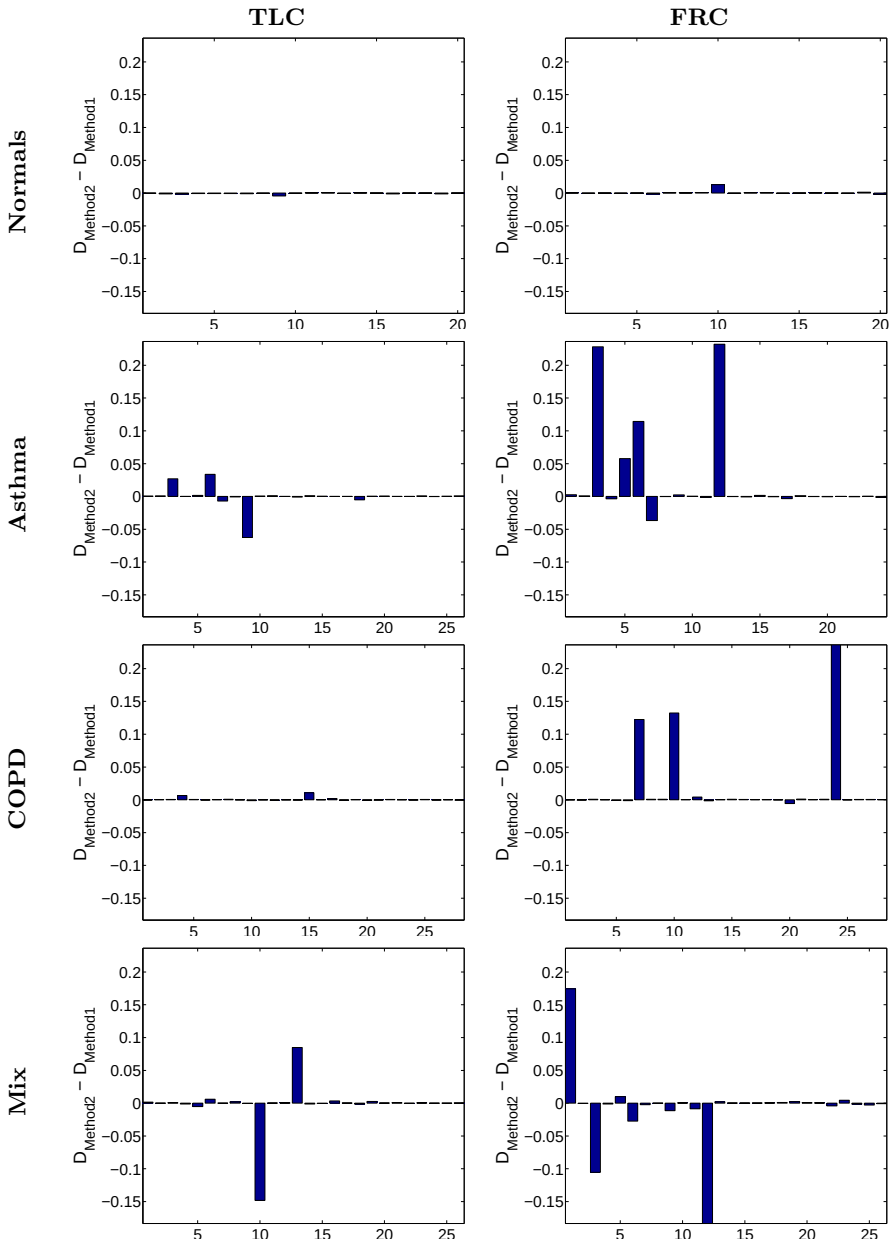

Fig. 6: Bar plots showing the difference in Dice coefficients between final lung segmentations generated based on initialization Method 2 and Method 1.

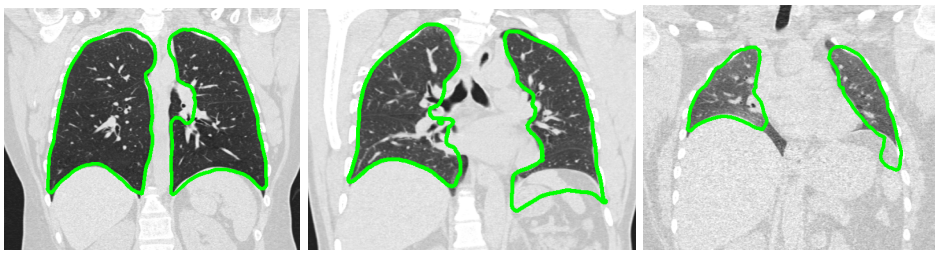

(a) Method 1

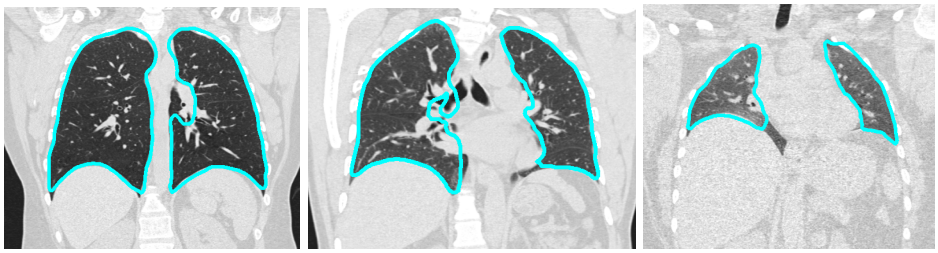

(b) Method 2

Fig. 7: RASM segmentations. Corresponding initial RASM shown in figure 1 for method 1 and figure 5 for method 2

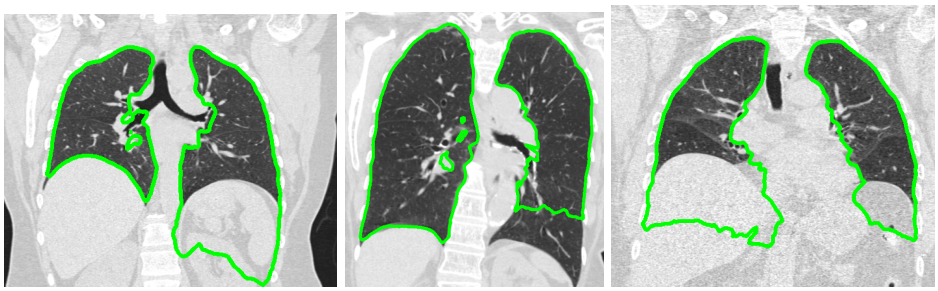

(a) Method 1

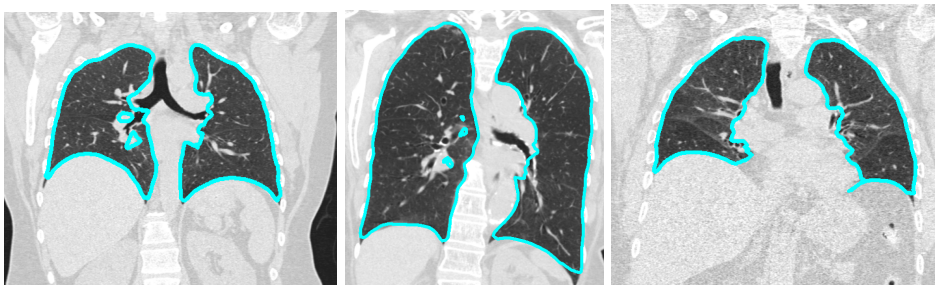

(b) Method 2

Fig. 8: RASM-OSF segmentations.

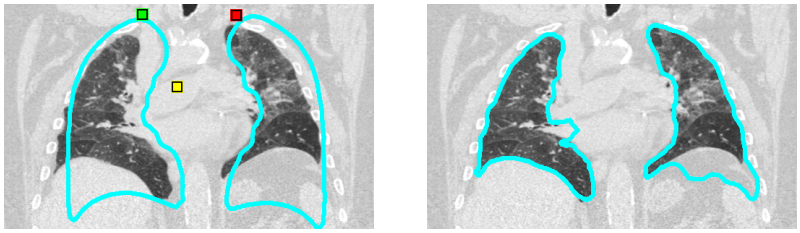

(a) (b)

Fig. 9: (a) Initial RASM overlaid with projections of the predicted lung apex and carina. (b) Final RASM-OSF segmentation

5 Discussion and Conclusions

With the presented work we have shown that a landmark-based initialization approach for our robust model-based lung segmentation method is feasible. The approach delivered good results across TLC and FRC CT scans as well as a range of different lung diseases. The overall performance of the the new method was found to be comparable to the previously utilized ribcage-based initialization system. In addition, the new method delivered improved results for many cases where the old approach failed (Fig. 6) and was found to be three times faster.

Currently the initialization system is based on predicting three landmark points (carina and left/right lung apex), which are then used to estimate scale and position of the initial RASM. The presented work represents an initial study with a only a small number of landmarks. However, the framework allows us to easily incorporate additional landmark points for a fraction of additional computing time. For example, landmarks on the diaphragm or the costophrenic angles could be used to improve the scale estimation of the initial RASM. This will very likely lead to a more robust model initialization and allow us to reduce remaining initialization inaccuracies. In other future work we will investigate options to combine FBA with point distribution models for direct initialization of RASM.

Acknowledgments. This work was supported in part by NIH NLBI Grant R01HL111453. ***R2B***

References

1. Cootes, T., Taylor, C., Cooper, D., Graham, J.: Active shape models-their training and application. Computer Vision and Image Understanding **61**(1) (January 1995) 38–59
2. Hu, S., Hoffman, E.A., Reinhardt, J.M.: Automatic lung segmentation for accurate quantitation of volumetric x-ray ct images. IEEE Transactions on Medical Imaging **20** (2001) 490–498

3. III, S.G.A., Sensakovic, W.F.: Automated lung segmentation for thoracic ct: Impact on computer-aided diagnosis1. Academic Radiology **11**(9) (2004) 1011 – 1021
4. Leader, J.K., Zheng, B., Rogers, R.M., Sciurba, F.C., Perez, A., Chapman, B.E., Patel, S., Fuhrman, C.R., Gur, D.: Automated lung segmentation in x-ray computed tomography: development and evaluation of a heuristic threshold-based scheme. Academic radiology **10**(11) (November 2003) 1224–1236
5. Pu, J., Paik, D.S., Meng, X., Roos, J.E., Rubin, G.D.: Shape "break-and-repair" strategy and its application to automated medical image segmentation. IEEE transactions on visualization and computer graphics **17**(1) (January 2011) 115–124
6. Sluimer, I., Prokop, M., van Ginneken, B.: Toward automated segmentation of the pathological lung in CT. IEEE transactions on medical imaging **24**(8) (August 2005) 1025–1038
7. Sonka, M., Hlavac, V., Boyle, R.: Image processing, analysis, and machine vision. Thompson Learning, Toronto (2008)
8. Sun, S., Bauer, C., Beichel, R.: Automated 3-d segmentation of lungs with lung cancer in ct data using a novel robust active shape model approach. IEEE Trans Med Imaging **31**(2) (2012) 449–60
9. Toews, M., Wells III, W.: Efficient and robust model-to-image alignment using 3d scale-invariant features. Medical Image Analysis **17**(3) (2013) 271–282
10. van Rikxoort, E.M., de Hoop, B., Viergever, M.A., Prokop, M., van Ginneken, B.: Automatic lung segmentation from thoracic computed tomography scans using a hybrid approach with error detection. Medical Physics **36**(7) (2009) 2934–2947
11. Wang, J., Li, F., Li, Q.: Automated segmentation of lungs with severe interstitial lung disease in CT. Medical physics **36**(10) (October 2009) 4592–4599